PNAS RESEARCH ARTICLE | MICROBIOLOGY

Unidirectional mannitol synthesis of *Acinetobacter baumannii* MtlD is facilitated by the helix–loop–helix-mediated dimer formation

Heng-Keat Tam[a,1,2], Patricia König[b,c], Stephanie Himpich[a], Ngoc Dinh Ngu[b,c], Rupert Abele[a], Volker Müller[b,c], and Klaas M. Pos[a]

Edited by Liang Tong, Columbia University, New York, NY; received April 29, 2021; accepted February 23, 2022, by Editorial Board Member Caroline S. Harwood

Persistence of *Acinetobacter baumannii* in environments with low water activity is largely attributed to the biosynthesis of compatible solutes. Mannitol is one of the key compatible solutes in *A. baumannii*, and it is synthesized by a bifunctional mannitol-1-phosphate dehydrogenase/phosphatase (AbMtlD). AbMtlD catalyzes the conversion of fructose-6-phosphate to mannitol in two consecutive steps. Here, we report the crystal structure of dimeric AbMtlD, constituting two protomers each with a dehydrogenase and phosphatase domain. A proper assembly of AbMtlD dimer is facilitated by an intersection comprising a unique helix–loop–helix (HLH) domain. Reduction and dephosphorylation catalysis of fructose-6-phosphate to mannitol is dependent on the transient dimerization of AbMtlD. AbMtlD presents as a monomer under lower ionic strength conditions and was found to be mainly dimeric under high-salt conditions. The AbMtlD catalytic efficiency was markedly increased by cross-linking the protomers at the intersected HLH domain via engineered disulfide bonds. Inactivation of the AbMtlD phosphatase domain results in an intracellular accumulation of mannitol-1-phosphate in *A. baumannii*, leading to bacterial growth impairment upon salt stress. Taken together, our findings demonstrate that salt-induced dimerization of the bifunctional AbMtlD increases catalytic dehydrogenase and phosphatase efficiency, resulting in unidirectional catalysis of mannitol production.

Acinetobacter baumannii | mannitol | compatible solutes | dehydrogenase | phosphatase

Significance

Mannitol biosynthesis is essential for *Acinetobacter baumannii* to cope with osmotic stress. Currently, only *Pseudomonas putida*, *Acinetobacter baylyi*, and *A. baumannii* are able to de novo synthesize mannitol by a structurally unique bifunctional mannitol-1-phosphate dehydrogenase/phosphatase (AbMtlD). The molecular mechanism of reduction and dephosphorylation of fructose-6-phosphate to mannitol is highly dependent on the substrate shuffling from one protomer to the other protomer by a unique helix–loop–helix domain–mediated dimer formation, thus ensuring unidirectional and efficient biosynthesis of mannitol. These observations support an evolutionary adaptation of AbMtlD by fusion of dehydrogenase and phosphatase domains to facilitate efficient unidirectional enzymatic production of mannitol, unifying regulatory control and minimizing the intracellular concentration of toxic mannitol-1-phosphate during salt stress.

The opportunistic human pathogen *Acinetobacter baumannii* has been recognized as the most critical clinical species by the World Health Organization in 2017, as it is the most prevalent multidrug-resistant gram-negative bacterium responsible for nosocomial infections (1). Persistence of *A. baumannii* in clinical settings is associated with intrinsic antibiotic resistance, ability to acquire antibiotic resistance, desiccation tolerance, biofilm formation, adherence to biotic and abiotic surfaces, and metabolic versatility (2–8). The increase in nosocomial infections by *A. baumannii* is largely attributed to its ability to acquire antibiotic resistance and long-term survival on dry surfaces (1, 8). *A. baumannii* uses several means to mitigate the damage from desiccation by enhancing water retention through the accumulation of compatible solutes, capsule formation, and biofilm formation (5, 9, 10). Considering the important role of desiccation survival in the persistence and dissemination of multidrug-resistant *A. baumannii* in the healthcare system, it is imperative to investigate the underlying molecular mechanism of biosynthesis of osmolytes.

Mannitol is the most abundant six-carbon noncyclic polyol in nature and is used as a carbon and energy source, compatible solute, and antioxidant in plants, fungi, and bacteria (11–14). Recently, it was proven that intracellular mannitol plays a key role in virulence and pathogenicity and contributes to maintaining intracellular water content in fungi and bacteria (14–16). Interestingly, only three bacterial species, *Pseudomonas putida*, *Acinetobacter baylyi*, and *A. baumannii* have been identified to synthesize mannitol (13, 17, 18). The synthesis of mannitol is catalyzed by mannitol-1-phosphate (M1P) dehydrogenase/phosphatase (MtlD), a bifunctional M1P dehydrogenase (DH)/phosphatase (PD) composed of an N-terminal PD domain belonging to the haloacid dehalogenase (HAD) superfamily and a C-terminal DH domain (13, 19). This enzyme catalyzes the first step of the reduction of fructose-6-phosphate (F6P) to M1P with NADPH as a reductant, followed by the dephosphorylation of M1P to mannitol (19). Interestingly, MtlD from *A. baumannii* (AbMtlD), as the key enzyme for mannitol biosynthesis, has a requirement for salt and high osmolarity (17, 20).

In this study, we determined the crystal structure of AbMtlD and uncovered the catalytic role of the helix–loop–helix (HLH) domain of AbMtlD. AbMtlD dimers are

The authors declare no competing interest.

This article is a PNAS Direct Submission. L.T. is a guest editor invited by the Editorial Board.

[1]Present address: Department of Medical Microbiology, Hengyang Medical School, University of South China, Hengyang 421002, China.

[2]To whom correspondence may be addressed. Email: tamhk60@hotmail.com.

This article contains supporting information online at http://www.pnas.org/lookup/suppl/doi:10.1073/pnas.2107994119/-/DCSupplemental.

Published April 1, 2022.

composed of a putative product/substrate tunnel and substrate-binding site connecting the DH and PD catalytic domains. Enzymatic assays revealed that the catalytic efficiency of engineered disulfide bond–crosslinked AbMtlD via the HLH domain increases significantly, corroborating a functional role of AbMtlD dimer formation. AbMtlD dimers appear to ensure unidirectional biosynthesis of mannitol from F6P, limiting the accumulation of free M1P during salt stress.

Results

Structure of MtlD. The structure of AbMtlD was initially determined by single-wavelength anomalous diffraction (SAD) using selenomethionine (Se-Met)-substituted protein to a resolution of 3.1 Å (*SI Appendix*, Table S1). The resulting model was used as a search model by molecular replacement to solve the structure of unliganded AbMtlD at 2.6 Å, substrate-bound AbMtlD, and an AbMtlD-D16A variant. All unliganded and substrate-bound AbMtlD structures were crystallized in space group $C222_1$, with two molecules per asymmetric unit, except for the crystal structure of M1P bound to AbMtlD-PD (discussed later). In contrast, data analysis of size-exclusion chromatography and native polyacrylamide gel electrophoresis (PAGE) indicated that AbMtlD exists predominantly in a monomeric state in the gel filtration buffer, and only a minor fraction appears as a dimer (*SI Appendix*, Fig. S7 *A* and *B*). Each of the AbMtlD protomers constitutes a three-domain structure comprising a HAD superfamily–conserved PD domain at the N terminus, a DH domain at the C terminus, and a small HLH domain, together forming a door–lever-like structure (Fig. 1*A* and *SI Appendix*, Fig. S1). The two protomers interact with each other via the intersecting HLH domains, forming an X-like AbMtlD dimer (Fig. 1*A*). In general, the intermolecular interactions of the intersecting HLH assembly in the AbMtlD dimer are organized by the "tip-to-base" and "body-to-body" interactions as well as interaction of HLH with the PD and DH domains from its dimeric partner (Fig. 1*A* and *SI Appendix*, Tables S2 and S3). Although the HLH domain is composed of multiple hydrophilic residues, the HLH assembly is mainly contributed by hydrophobic and van der Waals interactions (Fig. 1*A*, *Inset*, and *SI Appendix*, Table S2).

The PD domain of AbMtlD exhibits a typical HAD type I topology (21), comprising a core and a cap domain (*SI Appendix*, *Structural feature of the PD domain* and Figs. S1*A* and S2 *A* and *B* and Fig. 1*B*). To obtain M1P bound to the AbMtlD PD domain, the conserved catalytic residue D16 in the HAD family was substituted to alanine (21, 22). The AbMtlD-D16A variant crystallized in two AbMtlD dimers in the asymmetric unit with M1P bound to the catalytic sites of all PD domains. All four independent copies of the PD domain from this structure are structurally identical among not only each other but also the closed conformation (0.47 to 0.58 Å rmsd between C_α atoms; *SI Appendix*, Fig. S2*A*). This result suggests that the different crystal packing does not impose substantial differences to the PD domain. M1P binding facilitates a 24° rotation of the cap subdomain relative to the core subdomain, trapping the M1P complex in the active site (Fig. 1*B*).

In contrast to bacteria that catalyze mannitol synthesis with two separate enzymes (i.e., the M1P DH [M1PDH] and M1P PD [M1PP]) (23), the DH domain of AbMtlD is fused to the C terminus of the PD domain, forming a bifunctional DH/PD enzyme. The DH domain is atypical for a member of the long-chain DH/reductase (LDR) family, as it is composed of archetypal N- and C-terminal DH subdomains and, in addition, a unique HLH subdomain (residues 423 to 484, α17–loop–α18; Fig. 1*C* and *SI Appendix*, Figs. S1*B* and S3). This HLH subdomain is inserted between the N-terminal β15 and β16, which is absent in other LDR members (*SI Appendix*, Figs. S1*B* and S3). This unique feature is suggested to be involved in dimerization, with implications for enzymatic catalysis (*SI Appendix*, Fig. S1*B*). Structural analysis of the DH domain in the apo or substrate-bound state indicates that the C-terminal subdomains adopt open, intermediate, resting, or closed states, indicative of rigid body motion during catalysis (*SI Appendix*, *Structural feature of the DH domain*, *The binding mode of NADH and NADPH*, and Fig. S4*A* and Fig. 1*C*). Binding of F6P to the DH domain appears to induce a rotation of the C-terminal subdomain by ∼46° with respect to the N-terminal subdomain (Fig. 1*C*). This pendulum-like motion results in a closure of the intersubdomain cleft. The ternary complex of the DH domain in the presence of NADPH and F6P appears to represent the closed state, characterized by multiple intra- and intersubdomain hydrogen bonds (*SI Appendix*, *Structural feature of the DH domain* and Fig. S4 *B* and *C*). Taken together, we demonstrate that the AbMtlD DH domain, which is a member of the M1PDH family, adopts binary (e.g., M1P-, NADH-, or NADPH-bound) and ternary states (e.g., F6P/NADPH-bound; *SI Appendix*, *Structural feature of the DH domain*, *The binding mode of NADH and NADPH*, and Figs. S3 and S4*A*).

Binding of M1P to the PD domain. Although the crystallization condition included the presence of Mg^{2+} ions, M1P bound to the PD domain of full-length AbMtlD-D16A was crystallized in a closed conformation with no Mg^{2+} bound. In contrast, Mg^{2+} binding is observed proximal to D16 in wild-type AbMtlD, indicating the importance of D16 in Mg^{2+} coordination (Fig. 1*B* and *SI Appendix*, Fig. S5*A*). M1P binds to the active site composed of the N- and C-terminal subdomains of the PD domain (Fig. 1*B*). Here, M1P is positioned in a straight chain configuration, such that the phosphate and mannitol moieties make extensive contact with the core and cap subdomains, respectively (Figs. 1*B* and 2*A*). Upon M1P binding, the α2-turn-α3 region from the cap subdomain reorients toward the active site, and the sugar alcohol moiety is sandwiched by the α2-turn-α3 and α1 (*SI Appendix*, *Structural feature of the PD domain* and Figs. 1*B* and 2*A*). In general, the catalytic residues (D16, D18, T118, K151, E175, and D176) from the core domain are conserved in the HAD family (21) (*SI Appendix*, Fig. S1*A*) and are involved in phosphate and/or Mg^{2+} coordination, indicating the important role of these residues in the dephosphorylation of M1P. Additionally, main chain amides of M17, D18, and S119 are in interaction with the negatively charged phosphate moiety. Residues at the active site of the cap subdomain are highly distinct among the members of the HAD family (*SI Appendix*, Fig. S1*A*), as the cap domain is primarily involved in substrate specificity (24). In contrast, the core domain is structurally conserved, as this domain is important for phosphate binding and catalysis (24). Among the homologs of the AbMtlD PD domain, however, active site residues at the cap domain (E25, R28, L32, L53, Y74, R78, and S120) are conserved (*SI Appendix*, Fig. S1*A*). As described above, the α2-turn-α3 region is required to stabilize the closed conformation and involves direct recognition of the C3-OH and C5-OH of M1P by the main chain of C52, G54, and L55 (Fig. 2*A*). E85 coordinates R28 to interact with the C2-OH of M1P, and S120 interacts with M1P C2-OH. The C3-OH and C4-OH moieties of M1P are hydrogen bonded by the side chain of E25. Additionally, Y74 and D82 support the

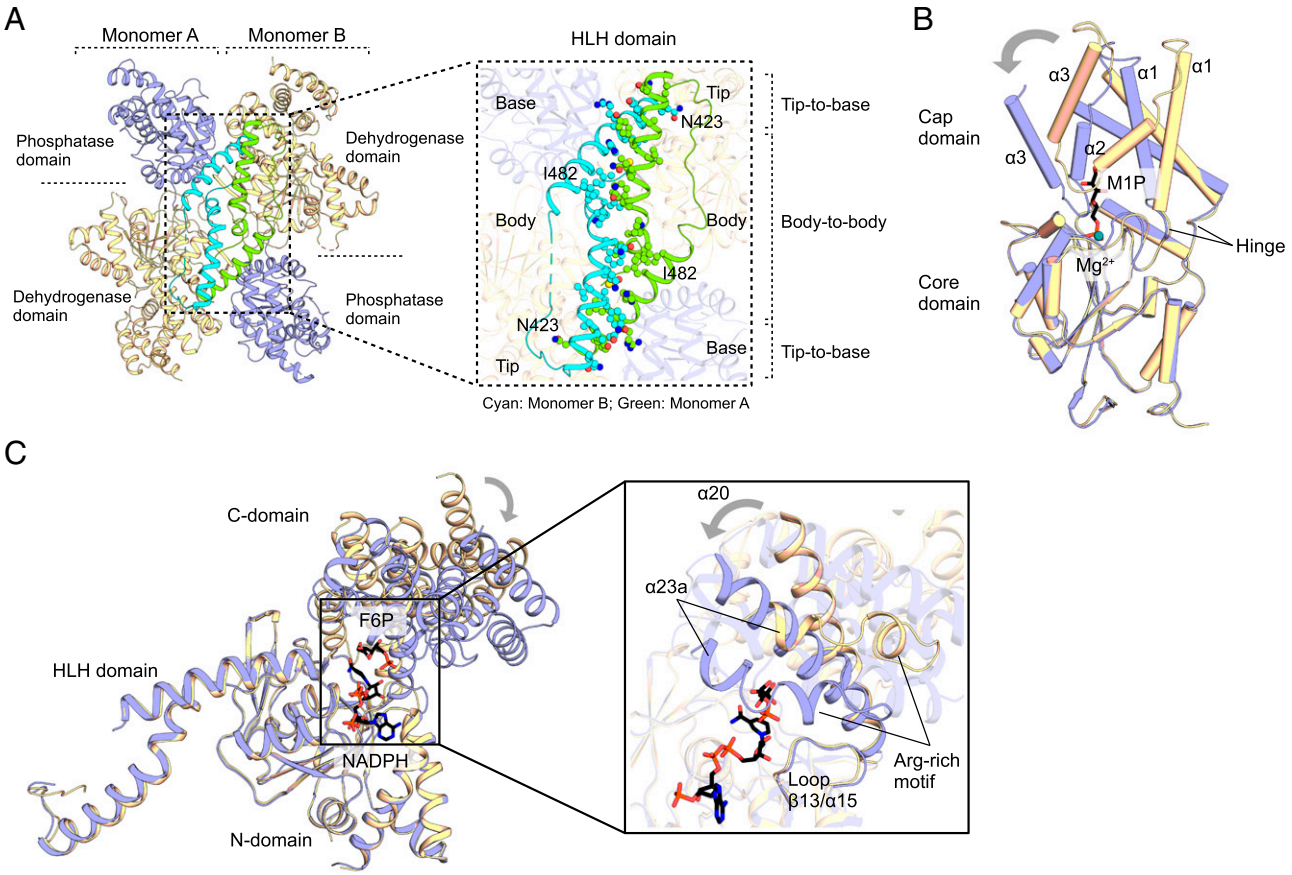

Fig. 1. Crystal structure of the AbMtlD. (*A*) Cartoon representation of dimeric AbMtlD (PD domain: blue; DH domain: wheat). The HLH domain (residues 423 to 486) is colored cyan (monomer B) and green (monomer A), respectively. The *Inset* depicts that the closest distances of C_α between residues in the body-to-body assembly of HLH domains are 4.8 to 6.6 Å, and the closest distances of C_α between residues in the tip-to-base assembly of HLH domains are 6.4 to 6.8 Å. For more details, refer to *SI Appendix*, Table S3. (*B*) PD domains in open (blue) and closed (wheat) states. Binding of M1P induces a 24° rotation of the cap domain relative to the core domain. Mg^{2+} binds only to the open state. (*C*) DH domains in open (blue) and closed (wheat) conformations. Binding of F6P induces a 46° rotation of the C terminus relative to the N terminus.

geometric position of the R78 side chain toward M1P, such that the guanidinium of R78 engages in a water-mediated interaction with the C2-OH and C5-OH moieties of M1P. Additionally, the C6-OH moiety of M1P interacts with the CO moiety of L49 via a water-mediated hydrogen bond. The conserved residue L53 in the bifunctional MtlD is involved in van der Waals interaction with the mannitol moiety, stabilizing M1P binding and preventing the release of M1P during catalysis (Fig. 2*A* and *SI Appendix*, Fig. S1*A*).

Binding of M1P/F6P and Cofactor to the DH. To understand the specificity of the AbMtlD DH activity, several ligand-bound binary and ternary structures of wild-type AbMtlD in the presence of NADPH, NADH, or F6P/NADPH were obtained. For solving the structure of the binary complex of M1P bound to the DH domain, the N374A variant was used. F6P or M1P bind to the active site cleft between the N- and C-terminal part of the DH domain with the sugar or sugar alcohol moiety positioned deep into the cleft. The F6P/M1P–binding site is defined by α20, α23a, α23b, loop β13/α15, and loop β14/β15 (*SI Appendix*, Fig. S1*B*). Interestingly, F6P binds in the extended configuration and not in the cyclic configuration (Fig. 2*C* and *SI Appendix*, Fig. S5*B*). Both F6P and M1P molecules adopt a bent chain configuration with a tilted phosphate moiety (*SI Appendix*, Fig. S5*B*). F6P is stacked parallel to the nicotinamide ribosyl moiety, allowing the C5 atom of F6P to be situated proximal to the nicotinamide C4 moiety (3.55 Å; Fig. 2*B* and *SI Appendix*, Fig. S6*A*). The phosphate moiety of F6P is instead solvent exposed and forms a hydrogen bond with the nicotinamide ribosyl moiety (Figs. 1*C* and 2 *B* and *C*). Furthermore, the negatively charged phosphate moiety of F6P is surrounded by four positively charged residues, namely R609, R613, K614, and R620 from the arginine-rich consensus motif ^{609}RxxxRKxxxx(E/D)R^{620} (Fig. 2*C*), stabilizing the bent conformation of the phosphate moiety. The arginine-rich motif is a unique characteristic of M1PDH for the selectivity of M1P over mannitol (*SI Appendix*, Fig. S1*B*). The bent conformation of F6P/M1P is mainly contributed by the movement of α23a (residues 604 to 608) and the side chain of K614 and R609 toward the phosphate moiety (Figs. 1*C* and 2 *C* and *D*), enforcing the tilted phosphate configuration. Of note, arginines from the arginine-rich consensus as well as the R606 are positioned as arginine-glutamine/asparagine (R613-Q339) or arginine-carboxylate (R606-D602 and R620-E619) pairs, resulting in an ideal arginine rotamer conformation for F6P binding (*SI Appendix*, Fig. S4*E*). Interestingly, these glutamine/asparagine or carboxylate residues are highly conserved among M1PDH except for MtlD from *A. baylyi* and M1PDH from *Salmonella enterica* that contain histidine and glycine at position 339, respectively (*SI Appendix*, Fig. S1*B*).

All the conserved residues located at the unique catalytic consensus ^{527}KxxxxNxxH^{535} for polyol-specific LDRs (PSLDRs) (25) are involved in the interaction with the F6P in AbMtlD. PSLDRs use lysine as a catalytic base rather than a metal ion or

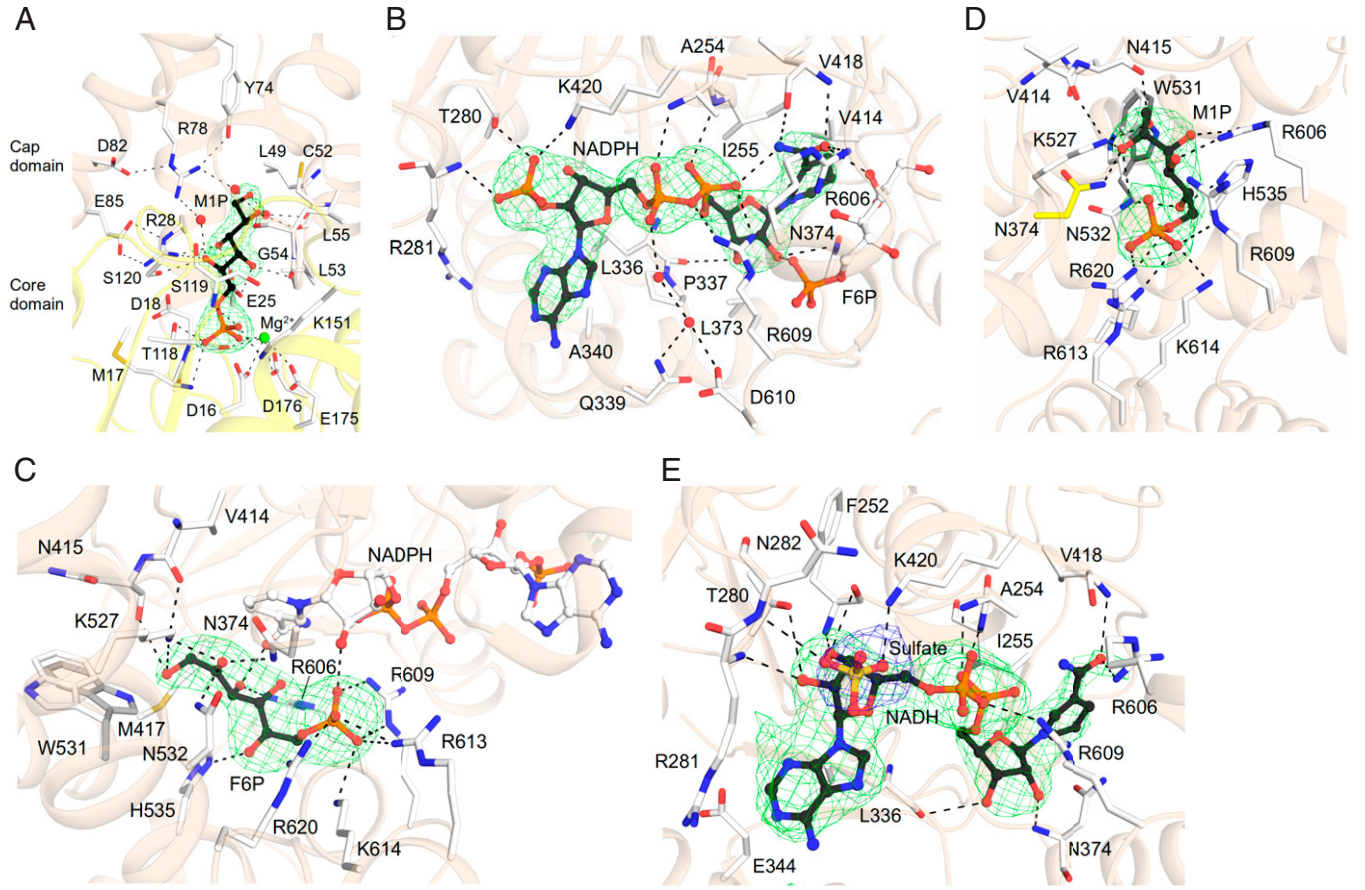

Fig. 2. Active site of the PD and DH domains. Water molecules are depicted as red spheres. (*A*) M1P binding to the D16A variant in the absence of Mg^{2+}. Both D16 and Mg^{2+} are modeled to the D16A structure. The Polder map of M1P was contoured at 6.5 σ. (*B*) NADPH binding to the closed state comprising F6P (monomer B of PDB ID 7OCR). The Polder map of NADPH was contoured at 6.0 σ. (*C*) Active site of F6P and NADPH in the closed state (monomer B of PDB ID 7OCR). W531 of unliganded AbMtlD is colored in gray. The Polder map of F6P was contoured at 6.0 σ. (*D*) M1P binding to the N374A mutant (monomer B of PDB ID 7OCU). N374 was modeled to the structure (*SI Appendix*, Fig. S5*C*). W531 of unliganded AbMtlD is colored in gray. The Polder map of M1P was contoured at 7.0 σ. (*E*) Binding of NADH and sulfate to the closed state (monomer B of PDB ID 7OCQ). The Polder map of NADH and sulfate was contoured at 4.5 and 6.5 σ, respectively.

tyrosine, as in the case of short-chain and medium-chain DHs. This result confirms that the DH domain of AbMtlD is related to the PSLDRs (25, 26). The hydroxyl moiety of F6P C5 forms hydrogen bonds with three residues (N374, K527, and N532; *SI Appendix*, *Active site of the DH domain* and Fig. S5*C* and Fig. 2*C*), whereas the C2-OH of F6P is coordinated by H535 (Fig. 2*C*). Interestingly, whereas N532 forms an additional hydrogen bond with C2-OH of M1P, this interaction is absent in the NADPH/F6P–bound ternary state (Fig. 2 *C* and *D*). Similar hydrogen bond interaction of N532 with C2-OH of M1P was also reported in mannitol-bound mannitol 2-DH from *Pseudomonas fluorescens* (PfM2DH), where N300 of PfM2DH interacts with C5-OH of mannitol (27). R606 from the ^{602}DxxxR^{606} consensus motif (*SI Appendix*, Fig. S1*B*) in M1PDH is involved in hydrogen bonding with both C3-OH and C4-OH of F6P/M1P except for C4-OH of F6P. Interestingly, D230 of PfM2DH, which is highly conserved in M2DH and M1PDH family members and coordinates with the mannitol C1-OH moiety, is replaced by N415 in AbMtlD, such that the N415 main chain carbonyl interacts with the C6-OH of M1P (C1-OH in mannitol; Fig. 2 *C* and *D* and *SI Appendix*, Fig. S1*B*) rather than the N415 side chain. Only two hydrophobic residues M417 and W531 are in close contact with C1 and C1-OH of F6P, respectively (Fig. 2 *C* and *D*). M417 is conserved only among the bifunctional MtlD from *Acinetobacter* species, but it is replaced by leucine in other M1PDHs and M2DHs (*SI Appendix*, Fig. S1*B*). Interestingly, binding of F6P/M1P facilitates a rotamer conformational change of W531, a conserved residue in bifunctional MtlD (Fig. 2*C* and *SI Appendix*, Fig. S1*B*), allowing the binding of F6P or M1P. In contrast, W531 is replaced by less bulky hydrophobic residues valine or leucine in other M1PDHs and M2DHs, indicating the importance of the tryptophan in the binding pocket of bifunctional MtlD (*SI Appendix*, Fig. S1*B*).

As in other PSLDRs, NADPH binds to a shallow cleft at the N terminus of the AbMtlD DH domain, comprising six-stranded parallel β-sheets, a canonical Rossmann fold (Fig. 1*C*). The NADPH is situated proximal to the F6P-binding site, such that the nicotinamide moiety is oriented proximal to F6P and sandwiched between F6P and I255 (Fig. 2*B*). Since NADPH binds in an identical position to the active site of the binary and ternary complexes in a closed state (blue in *SI Appendix*, Figs. S4*A* and S6 *A* and *B*), only NADPH bound to the ternary complex in the closed state will be discussed, unless specified (*SI Appendix*, *The binding mode of NADH and NADPH*). The sugar pucker of both adenosine and nicotinamide ribosyl moieties adopts a C2′-endo/C3′-exo conformation. The nicotinamide ring is oriented in *syn* conformation, facilitating an intramolecular hydrogen-bond interaction with the pyrophosphate moiety (Fig. 2*B*). The amide oxygen of nicotinamide forms three hydrogen bonds with R606 (conserved residue), the V418 main chain NH (conserved residue), and the F6P C3-OH moiety. Additionally, the main chain

CO moiety of V418 interacts with the amide nitrogen atom of nicotinamide. The nicotinamide ribosyl C2-OH moiety engages in hydrogen bonds with F6P phosphate, the N374 side chain amide, and the L336 main chain carbonyl moieties (*SI Appendix*, *Active site of the DH domain* and Fig. 2*B*).

The pyrophosphate moiety is positioned at the N terminus of α11, comprising a glycine-rich motif (^{249}IHGFGAIGGGY^{259}; Fig. 2*B* and *SI Appendix*, Figs. S1*B*, S4*D* and S6*B*). Interestingly, the glycine-rich motif of the DH domain shows a variation to the canonical glycine-rich motif found in LDR family members (xHxGxGxxxRx) (27), with a conserved histidine residue preceding the conserved GxG motif and a glycine instead of an arginine at position 257 (*SI Appendix*, Fig. S1*B*). The three consecutive glycine residues together with the Y259 (^{256}GGGY^{259}) in the DH domain form a rather unusual π-helix within the α11. Furthermore, Y295 and the invariant R416 within the conserved motif ^{414}V(D/N)RxV^{418} interact with the carbonyl moiety of G257 and G258 from the π-helix, respectively (*SI Appendix*, Fig. S6*C*). R416 is further stabilized by a hydrogen-bond network involving Q262, Y299, S493, and D496. These unique features enable the amide of A254 and I255 from the glycine-rich motif to interact with the pyrophosphate by hydrogen bonding. R609 from the conserved ^{606}RVxR^{609} motif plays a dual function, as shown in interaction with the phosphate moiety of F6P/M1P, and interacts with the pyrophosphate of NADPH (Fig. 2 *B*–*D*). Additionally, the negative charges of the pyrophosphate are compensated by the hydrogen-bond network composed of Q339 and D610 via two water molecules (Fig. 2*B*).

The adenine base of NADPH is sandwiched by R281 from one side and by L336, P337, and A340 from another side (Fig. 2*B*). The presence of a positively charged residue (K420) and a main chain amide and the absence of a negatively charged residue (D69 in PfM2DH) (27) near the C2′O-phosphate of the adenosine ribosyl moiety suggests that the DH domain of AbMtlD has a clear preference for NADPH over NADH (Fig. 2 *B* and *E*). Indeed, T280 and K420 of AbMtlD interact and stabilize the negatively charged phosphate moiety of NADPH (Fig. 2*B*). Additionally, loop β8/α12 composed of R281 and N282 residues is positioned in such a way that the main chain amide moieties of these residues are facing the C2′O-phosphate moiety. Nevertheless, a clear electron density assigned to NADH was observed at the cofactor-binding pocket of the DH domain in the closed state (Fig. 2*E* and blue in *SI Appendix*, Fig. S4*A*) but not in the resting state (orange in *SI Appendix*, Fig. S4*A*) when unliganded AbMtlD crystals were soaked with 5 mM NADH (similar concentration as for NADPH), indicating that the DH domain of AbMtlD can bind NADH. Indeed, AbMtlD catalyzes the reduction of F6P with NADH (K_m = 1.73 ± 0.30 mM), and the specificity constant (k_{cat}/K_m) for NADH is 20-fold lower than that of NADPH (Table 1), indicating that AbMtlD exhibits a higher specificity for NADPH. The binding mode of NADH in the closed state is nearly identical to the NADPH-binding mode, apart from those residues that are involved in the interaction with the NADPH C2′O-phosphate moiety (*SI Appendix*, *The binding mode of NADH and NADPH* and Figs. S4*A* and S6*D* and Fig. 2 *B* and *E*).

Kinetics of the Active Site Mutants and the Importance of the HLH Domain in Catalysis. Kinetic determination of F6P reduction for AbMtlD resulted in K_m values of ∼60.6 mM and 192.0 μM for F6P and NADPH, respectively (Table 1 and *SI Appendix*, *Kinetic analysis of the DH domain*), consistent with a previous report for the F6P reduction activity (20). AbMtlD did not reduce glucose-1-phosphate. In contrast, a clear attenuated activity for glucose-6-phosphate reduction was observed with a slightly decreased K_m value but discernible decreased k_{cat} and k_{cat}/K_m values by 580- and 200-fold, respectively, compared to F6P reduction (Table 1). Taken together, the position of the phosphate and the carbonyl moieties on the hexose phosphate appear to be decisive for catalysis by AbMtlD (*SI Appendix*, *Kinetic analysis of the DH domain*).

The binding pocket of the DH domain is surrounded mainly by hydrophilic and charged residues, except for two hydrophobic residues M417 and W531, which are not conserved among M1PDH and M2DH (Fig. 2*C* and *SI Appendix*, Fig. S1*B*). The M417A variant exhibited comparable K_m and k_{cat}/K_m

Table 1. Kinetic parameters of AbMtlD F6P reduction activity and PD activity

Fructose-1-phosphate reduction activity*,†

	NADPH		
Variants	K_m (μM)	k_{cat} (s^{-1})	k_{cat}/K_m (μM^{-1} s^{-1})
WT	192.00 ± 45.00	141.20	0.735
D16A	153.00 ± 35.00	365.03	2.380
R609A	222.00 ± 24.00	8.16	0.037

	NADH*,†		
	K_m (μM)	k_{cat} (s^{-1})	k_{cat}/K_m (μM^{-1} s^{-1})
WT	1732.00 ± 297.00	61.98	0.036

	F6P*,†		
	K_m (mM)	k_{cat} (s^{-1})	k_{cat}/K_m (mM^{-1} s^{-1})
WT	60.59 ± 9.01	144.69	2.388
D16A	49.54 ± 5.78	256.56	5.179
M417A	35.55 ± 4.00	64.95	1.827
W531A	1.30 ± 0.14	93.85	72.192
D602A	41.31 ± 9.89	0.17	0.004
R606A	n.d.	n.d.	n.d.
R609A	56.46 ± 23.85	4.55	0.081
R613A	44.12 ± 15.49	29.35	0.665
K614A	n.d.	n.d.	n.d.
R620A	15.79 ± 4.18	0.15	0.009
ΔHLH	n.d.	n.d.	n.d.
A466C	65.49 ± 8.97	156.52	2.390
Y427C	128.27 ± 31.93	47.27	0.369
A466C-Y427C	16.23 ± 2.51	2,256.91	139.058
Y469C	233.62 ± 99.49	60.79	0.260
H434C-Y469C	11.80 ± 2.48	1,758.00	148.983

	WT (NADPH)*,†		
	K_m (mM)	k_{cat} (s^{-1})	k_{cat}/K_m (mM^{-1} s^{-1})
Glucose phosphate reduction activity			
Glucose-6-phosphate	21.67 ± 6.95	0.25	0.012
Glucose-1-phosphate	n.d.	n.d.	n.d.

	M1P*,†		
	K_m (mM)	k_{cat} (s^{-1})	k_{cat}/K_m (mM^{-1} s^{-1})
Mannitol-1-phosphate dephosphorylation activity			
WT	0.56 ± 0.09	152.88	273.000
D16A	n.d.	n.d.	n.d.

*Refer to Dataset S1 for curve fitting.
†n.d., not detected; WT, wild-type.

values for F6P and a mildly reduced k_{cat} only by twofold (Table 1). Surprisingly, the W531A variant exhibited a ∼50-fold decrease in K_m and 30-fold increase in k_{cat}/K_m for F6P (Table 1). W531A might augment the size of the binding pocket associated with alleviating the steric hindrance caused by the bulky W531 side chain, as shown in wild-type AbMtlD, to accommodate the F6P binding. It should be noted that W531 adopts a distinct conformation depending on the presence or absence of F6P in wild-type AbMtlD (Fig. 2 *C* and *D*). Therefore, we speculate that W531 might be involved in substrate specificity, such that only F6P is selected for catalysis.

The arginine-rich and ^{602}DxxxR^{606} motifs are involved in both F6P/M1P and NADPH binding (Fig. 2). To our surprise, R606A and K614A variants had no detectable F6P reduction activity (Table 1). In contrast, D602A, R609A, and R613A exhibited a similar or slightly lower K_m than the wild-type AbMtlD. However, a dramatic decrease in k_{cat}/K_m values was observed for these variants, except for R613A. The catalytic efficiency observed with the D602A and R609A variants was reduced by ∼600- and 30-fold, respectively. Compared with the wild-type AbMtlD, the R613A variant showed a comparably smaller decrease in k_{cat}/K_m by 3.6-fold. In contrast, the R620A variant exhibited a decrease of k_{cat}/K_m by a factor of 265. In sum, a significant decrease in catalytic efficiency was observed following substitution of the conserved charged residues, which interact with the phosphate moiety of F6P and are unequivocally important in binding and/or stabilizing the F6P upon catalysis (Fig. 2).

To address the functional coupling of both the PD and DH domains, we selectively inactivated the PD domain of AbMtlD by alanine substitution of D16, as D16 is an important catalytic residue for the PD activity (21, 22). The D16A variant exhibited a lack of PD activity but displayed noticeable F6P reduction activity (Table 1). Of note, the k_{cat}/K_m values for F6P and NADPH are 2.2- and 3.2-fold higher for the D16A variant than for the wild-type AbMtlD, respectively. As described above, AbMtlD is present as a monomer in gel filtration buffer composed of 20 mM 2-[4-(2-hydroxyethyl)-1-piperazinyl]-ethanesulfonic acid (HEPES) pH 7.5, 300 mM NaCl, and 5 mM β-mercaptoethanol, and substitution of the buffering agent (HEPES versus Tris) does not promote AbMtlD dimerization (*SI Appendix*, Figs. S7 *A* and *B* and S11 *A* and *B*). However, structural analysis of AbMtlD predicates dimer formation associated with the overt intersection of the HLH domain across each of the protomers (Fig. 1*A*). In support of this observation, size-exclusion chromatography coupled with multiangle light scattering (SEC-MALS) under high-salt conditions (600 mM NaCl) indicated a predominantly dimeric state (*SI Appendix*, Fig. S11*C*). We therefore hypothesize that the HLH domain is important in proper assembly of AbMtlD catalytic dimer formation. To address the functionality of the HLH domain in dimer assembly and catalysis, the HLH domain was replaced by a six-residue glycine-serine (GSGSGS) linker into positions 423 to 486 of AbMtlD (*SI Appendix*, Fig. S1*B*). To our surprise, removal of the HLH domain (ΔHLH) from AbMtlD showed a concomitant increase in dimer formation but a complete lack of F6P reduction activity, indicating that HLH-less dimeric AbMtlD is not active (Table 1 and *SI Appendix*, Fig. S7 *A* and *B*). As described above, the intersection of HLH domains is assembled in tip-to-base and body-to-body formations (Fig. 1*A*, *Inset*). The replacement of HLH with a short glycine-serine linker might impose a protein-folding constraint on dimer formation, resulting from a lack of the tip-to-base and body-to-body assemblies that maintain a productive dimer. Therefore, we speculate that AbMtlD lacking the HLH domain might form an improperly folded dimer, resulting in an inactive protein. This result prompted us to ask whether HLH-mediated dimer formation is functionally important in the catalysis of AbMtlD. To determine the importance of dimeric AbMtlD, we additionally constructed three pairs of double-cysteine mutants (A291C_R474C, Y427C_A466C, and H434C_Y469C), which are expected to form intermolecular disulfide-bonded cross-links (the distance of C_β between each cysteine pairs is ≤5.5 Å) between the intersected HLH domains from each protomer, respectively (Fig. 3*A*). Biochemical analysis by size-exclusion chromatography and native PAGE revealed the formation of protein dimers (Y427C_A466C and H434C_Y469C variants), indicating intermolecular thiol cross-linking of the intersected HLH domains (*SI Appendix*, Fig. S7 *A* and *C*). In contrast, the A291C_R474C variant was prone to form aggregates and was therefore excluded from this study. Both thiol–cross-linked A466C_Y427C and H434C_Y469C variants displayed higher F6P reduction activity (∼60-fold higher in k_{cat}/K_m) than wild-type AbMtlD (Table 1), whereas the single-cysteine variants (A466C, Y427C, and Y469C) exhibited similar or slightly lower k_{cat}/K_m values for F6P reduction activity, except for the H434C variant, however, which exhibited ambiguous activity. Taken together, these results indicate that the HLH domain forming the intersection within the AbMtlD dimer is functionally important in catalysis and might play a role in substrate transfer from the active site of the DH domain in monomer A to the active site of the PD domain in monomer B or vice versa (Fig. 3*C* and *SI Appendix*, Fig. S8). Interestingly, we observed a putative substrate/product–shuttling tunnel extending from the "initial" binding site at the DH domain to the "final" binding site at the PD domain (Fig. 3*C*). Within this putative tunnel, a HEPES molecule composed of a negatively charged sulfonate oxyanion moiety (similar to the phosphate moiety of M1P or F6P) was found to bind at the interface of HLH, DH, and PD domains (HDP interface) and was surrounded by positively charged and hydrophilic residues (Fig. 3 *B* and *C* and *SI Appendix*, Fig. S9). Therefore, the observed binding site for HEPES might suggest a possible binding site for M1P or F6P at the HDP interface (Fig. 3 and *SI Appendix*, Fig. S9). In an attempt to interfere with putative substrate/product shuttling, we conducted substitution analysis on residues lining the tunnel. No DH activity could be observed for the purified I130M, R298A-K433A-H492A, and S419L, whereas the L421M variant resulted in active DH and PD activities.

Toxicity of M1P in *A. baumannii*. D16, E175, and D176 of the HAD family are conserved catalytic residues for the PD activity (21, 22). Alanine substitution of these residues will inactivate the M1P dephosphorylation, as supported by our findings, indicating that the single D16A substitution variant displays a lack of PD activity (Table 1). To address the toxicity of M1P in *A. baumannii*, we expressed plasmid-borne single- (D16A), double- (D16A_D176A), and triple-alanine (D16A_E175A_D176A) AbMtlD PD domain substitution variants in the *A. baumannii* Δ*mtlD* strain grown in high-salt medium under the control of their native promoters, respectively. It was previously demonstrated that *mtlD* expression is modulated by high osmolarity (20). *A. baumannii* harboring the D16A variant was significantly impaired in growth under salt stress compared to the wild-type strain (*SI Appendix*, Fig. S10*A*). Confoundingly, double- and triple-alanine AbMtlD substitution completely abolished bacterial growth (*SI Appendix*, Fig. S10*A*). In contrast, these variants were not affected in growth devoid of NaCl

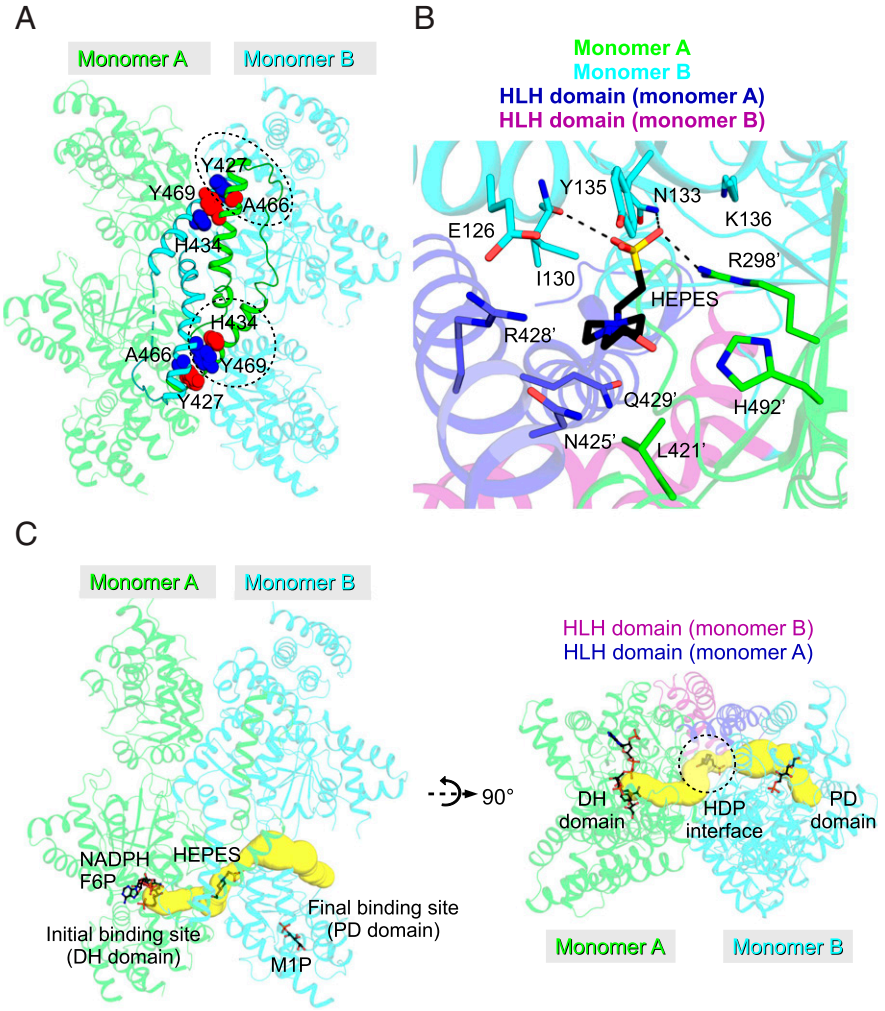

Fig. 3. Catalytically productive AbMtlD dimer. (*A*) Visualization of the engineered disulfide bonds. Locations of the engineered disulfide bonding are indicated by circles; residues from monomer A, red; residues from monomer B, blue. (*B*) Binding of HEPES to the HDP interface. (*C*) Formation of a putative substrate tunnel across the dimeric AbMtlD, extending from the DH domain of monomer A to the PD domain of monomer B via the HDP interface. The tunnel was calculated by Caver 3.0 (43).

(*SI Appendix*, Fig. S10*A*). Furthermore, the intracellular accumulation of M1P increased significantly in *A. baumannii* Δ*mtlD* complemented with the plasmid-borne double- or triple-alanine AbMtlD variants, but M1P only increased slightly in the D16A variant (*SI Appendix*, Fig. S10*B*). Taken together, these results verified a decisive role of M1P production by AbMtlD variants with an inactive PD domain in cell death.

Discussion

Bacteria use either the M1PDH/M1PP or M2DH pathway for mannitol metabolism as well as for maintaining the intracellular mannitol pool (23). Since mannitol is an important metabolite for *Acinetobacter* to challenge osmotic stress (10, 17), gene fusion of two distinct catalytic domains of M1PDH and M1PP might gain an advantage for *Acinetobacter* in response to low water activity without undergoing the regulation of two different proteins. In addition, gene fusion might also enhance the catalysis of both catalytic domains by efficient transfer of the M1P intermediate to the PD domain of AbMtlD. Since it is assumed that M1PDH reversibly catalyzes the reduction (F6P) and oxidation (M1P) reactions (14, 28), the unique fusion protein enables a rapid turnover of F6P to mannitol in a unidirectional fashion, devoid of M1P oxidation during mannitol synthesis. Furthermore, the conversion of M1P to mannitol is fostered efficiently intracellularly, as accumulation of a high concentration of the sugar phosphate like M1P is toxic to the cells (29, 30). In fact, the intracellular accumulation of toxic M1P increased in the *A. baumannii* Δ*mtlD* strain harboring the plasmid-borne inactive AbMtlD PD domain variants, leading to bacterial cell death (*SI Appendix*, Fig. S10). Taken together, these data verified the PD domain of AbMtlD to be functionally essential in *A. baumannii*, likely because of its function to catalyze conversion of the noxious M1P to a nontoxic and essential mannitol.

Intracellular ionic strength (K^+, Na^+, Mg^{2+}, Ca^{2+}, and Cl^-) in bacteria varies between 130 and 273 mM, and bacteria increase their intracellular osmolarity during osmotic stress (31–33). Notably, the *mtlD* expression and the enzymatic activity of AbMtlD in *A. baumannii* is highly regulated under osmotic shock (20). We therefore propose that AbMtlD forms a salt-induced catalytic productive AbMtlD transient dimer during catalysis to foster an efficient F6P reduction to M1P and subsequent dephosphorylation to mannitol (Fig. 3*A*, Table 1, and *SI Appendix*, Fig. S8). In fact, our results demonstrated that the intermolecular (with HLH domain) thiol–cross-linked variants exhibit higher F6P reduction activity than wild-type AbMtlD, supporting the functional relevance of HLH intersection across

each protomer in catalysis (Table 1). It is worth noting that the monomer–dimer equilibrium shifts toward AbMtlD dimer in the presence of high salt concentrations (*SI Appendix*, Fig. S11 *A* and *C*). This result suggested that AbMtlD exists most likely in a dimeric state in our enzymatic assay, which comprises a high NaCl concentration (600 mM NaCl) compared to the gel filtration buffer (300 mM NaCl; *AbMtlD Overproduction and Purification* and *DH Assay*). Notably, the initial cation concentration (e.g., Na^+ and K^+) in the protein crystallization droplet ranges between 270 and 370 mM, and the droplet undergoes vapor equilibrium, increasing eventually the cation concentration, inducing AbMtlD dimerization. Taken together, our findings implied that the HLH domain associated with catalytic productive dimer formation in a high osmolarity environment ensures that the mannitol synthesis is efficient and unidirectional.

Since there is a paucity of knowledge on the role of osmolytes in desiccation tolerance and osmoprotection, understanding the role of osmolyte biosynthesis in these processes may lead to better development of the sanitizing strategy to prevent infections as well as developing effective treatments against *A. baumannii* infections. In conclusion, this study provides detailed structural and enzymatic information of AbMtlD and proposes a unique catalysis involving formation of the HLH-mediated catalytic productive dimer. Moreover, the accumulation of M1P by an inactive PD domain of AbMtlD causes a growth impairment in *A. baumannii*. These data will facilitate the development of inhibitors targeting the mannitol biosynthesis pathway.

Methods

Site-Directed Mutagenesis. pET21AbMtlD$_{His}$ (20) was used as template for site-directed mutagenesis. Amino acid substitution was achieved using the ExSite protocol (Stratagene) with 5′-phosphorylated primers (*SI Appendix*, Table S4). Mutations were verified by sequencing (GATC Biotech).

AbMtlD Overproduction and Purification. A single colony of *Escherichia coli* BL21 (DE3) harboring pET21AbMtlD$_{His}$ (20) was inoculated in Lennox broth (LB) medium supplemented with 100 μg/mL ampicillin and grown overnight at 37 °C. Overnight cultures were inoculated into fresh LB medium supplemented with 100 μg/mL ampicillin and cultivated at 37 °C until an optical density at 600 nm (OD_{600}) of 0.5 to 0.6 was reached, and induction was performed with 0.3 mM isopropyl β-D-1-thiogalactopyranoside (IPTG; final concentration). Cultures were further grown at 16 °C for 18 h. Cells were harvested by centrifugation and suspended in buffer A (50 mM Tris pH 7.5, 500 mM NaCl, 20 mM imidazole, 10% glycerol, and 0.2 mM diisopropyl fluorophosphate) and disrupted twice with a pressure cell homogenizer (Stansted). Insoluble debris was removed by centrifugation at 160,000 × *g* for 45 min. Supernatant was loaded onto a HisTrap HP Ni^{2+} affinity column (GE Healthcare). After two washing steps with buffer A supplemented with the addition of 30 mM and 50 mM imidazole, respectively, proteins were eluted with the same buffer supplemented with the addition of 230 mM imidazole. Finally, concentrated protein was polished with buffer B (20 mM HEPES pH 7.5, 300 mM NaCl, and 5 mM β-mercaptoethanol) in a Superdex 200 10/300 GL column (GE Healthcare).

Crystallization of AbMtlD and AbMtlD Substitution Variants. Initially, crystals of AbMtlD were obtained by the sitting drop vapor diffusion method within 1 wk at 18 °C by equal volume of the protein solution (5 mg/mL) in the presence of 5 mM mannitol and the precipitant solution containing 0.15 to 0.25 M NaI and 20% PEG3350. Crystals were harvested and crushed with seed bead in mother liquor comprising 0.25 M NaI and 20% PEG3350 to prepare a 1:2,000 ratio of seed dilution for seeding experiments. Well-diffracting crystals were obtained by the sitting drop vapor diffusion method at 18 °C within 1 to 2 wk in precipitant solution containing 0.1 M Bis-Tris propane pH 6.5, 0.15 to 0.25 M Na_2SO_4, 0.2 M NaBr (can be substituted with 0.1 M potassium acetate or 0.1 M KI), 0.02 M $MgCl_2$, and 14 to 18% PEG3350) with a ratio of 3:2:1 or 2:3:1 of protein (5 mg/mL):precipitant:seed dilution. Crystals of different protein–substrate complexes were obtained by either cocrystallization using the same method as described above or via a soaking experiment described below. For cocrystallization experiments, protein solution (5 mg/mL) was mixed with appropriate amounts of substrates (described below), and the protein–substrate complexes were centrifuged at 13,000 × *g* for 10 min to remove any precipitates before setting up the crystallization. Soaking experiments were performed by soaking crystals in precipitant solution in addition to 5% glycerol and appropriate amounts of AbMtlD substrates (described below).

To obtain the crystals of AbMtlD-D16A in complex with M1P, AbMtlD-D16A protein solution was mixed with 50 mM M1P. To obtain the M1P-bound AbMtlD-N374A structure, a cocrystallization experiment was performed with AbMtlD-N374A in the presence of 100 mM M1P. To obtain the NADH-bound AbMtlD structure, unliganded AbMtlD crystals were soaked with 5 mM NADH overnight. To obtain the NADPH- and F6P-bound AbMtlD structure, AbMtlD was initially cocrystallized with 100 mM mannitol, and cocrystals were subsequently soaked with 75 mM F6P and 5 mM NADPH for 1 d. To obtain the NADPH-bound AbMtlD structure, AbMtlD was initially cocrystallized with 15 mM F6P, and, subsequently, cocrystals were soaked with 15 mM F6P and 5 mM NADPH for 1 d. To obtain the NADPH-bound AbMtlD-N374A structure, AbMtlD-N374A was initially cocrystallized with 50 mM M1P. Cocrystals of the M1P–AbMtlD-N374A complex were subsequently soaked with 50 mM M1P and 7.5 mM NADPH for 2 d. Crystals were serially transferred to cryoprotectant in mother liquor in addition to 5% and 15% glycerol, respectively, and flash-cooled in liquid nitrogen.

Se-Met Protein Production and Crystallization. A single colony of *E. coli* BL21 (DE3) harboring pET21AbMtlD$_{His}$ was inoculated in 5 mL of LB medium supplemented with 100 μg/mL ampicillin and grown for 6 h at 37 °C. Cultures were then inoculated into M9 minimal medium supplemented with 0.4% glucose, trace elements, and vitamins (34) in addition to 100 μg/mL ampicillin and grown for 16 h at 37 °C. Cells were harvested by centrifugation, and the cell pellet was inoculated into 1 L of fresh M9 minimal medium, as described above, and grown at 37 °C until an OD_{600} of 0.5 to 0.6 was reached. Cells were cooled on ice for 15 min before addition of 0.1 g of lysine, 0.1 g of threonine, 0.1 g of phenyalanine, 0.05 g of leucine, 0.05 g of isoleucine, 0.05 g of valine, and 0.05 g of L-(+)-selenomethionine, and cells were grown at 16 °C for an additional 15 min. Induction was performed with 0.5 mM IPTG (final concentration), and cultures were further grown at 16 °C for 18 h. Protein purification was performed as described above, but all purification buffers were supplemented with 5 mM β-mercaptoethanol throughout the whole purification procedure. Crystallization and cryoprotection of crystals were carried out as described above.

Diffraction Data Collection, SAD Phasing, and Refinement. Data were collected on beam line PROXIMA 1 (Eiger X 16M detector) and PROXIMA 2A (Eiger X 9M detector) at SOLEIL Synchrotron, Saint Aubin, France, and were indexed and integrated with XDS (35). The initial phase (3.1-Å dataset) was determined by the CRANK2 pipeline (36). All structural models were iteratively built in COOT (37) and refined with REFMAC5 (38) or BUSTER (Global Phasing). The structure was validated with MolProbity (39). Polder maps were calculated by phenix.polder (40). All figures were generated in PyMOL. Data collection and refinement statistics are listed in *SI Appendix*, Table S1.

DH Assay. Determination of the Michaelis–Menten kinetic parameters of the DH activity of AbMtlD was performed by following the time-dependent oxidation of NADPH at an absorbance of 340 nm by using a Tecan microplate reader (Tecan) as previously described (13). Briefly, the reaction was carried out at 34 °C in a total volume of 200 μL containing 50 mM MOPS pH 7.5, 600 mM NaCl, F6P, NADPH, and AbMtlD. To determine the kinetics for NADPH, ∼0.01 to 0.03 mg/mL AbMtlD was incubated with 70 mM F6P and various concentrations (0.01 to 1.0 mM) of NADPH. To determine the kinetics for F6P, ∼0.01 to 0.03 mg/mL AbMtlD, except for the AbMtlD variants (N374A, K527A, N532A, H535A, D602A, and R620A with concentrations of 0.1 to 0.13 mg/mL), was incubated with 0.1 mM NADPH and various concentrations (0.47 to 170 mM) of F6P. Initial enzymatic velocity of each measurement was determined after a 2-min reaction by fitting the data to the equation $V = \Delta[\text{NADPH}]/(\Delta t \times [\text{AbMtlD}])$, where $\Delta[\text{NADPH}]$ is the concentration difference of NADPH within the incubation time, Δt is the incubation time, and [AbMtlD] is the concentration of AbMtlD in the

reaction. Michaelis–Menten kinetics were calculated by fitting the data to the $Y = Et \times k_{cat} \times X/(K_m + X)$ function using GraphPad Prism 9.3.0.

PD Assay. PD activity was determined using the EnzChek phosphate assay kit (E-6646, Invitrogen) with a Tecan microplate reader (Tecan). Briefly, the reaction containing ~0.02 mg/mL AbMtlD was carried out at 28 °C in a total volume of 200 μL according to the manufacturer's instructions in the presence of various concentrations (25 to 1,400 μM) of M1P. Initial enzymatic velocity of each measurement was determined after a 1-min reaction by fitting the data to the equation $V = \Delta[MESG]/(\Delta t \times [AbMtlD])$, where Δ[MESG] is the concentration difference of 2-amino-6-mercapto-7-methyl-purine riboside (MESG) within the incubation time, Δt is the incubation time, and [AbMtlD] is the concentration of AbMtlD in the reaction. Michaelis–Menten kinetics were calculated by fitting the data to the $Y = Et \times k_{cat} \times X/(K_m + X)$ function using GraphPad Prism 9.3.0.

Growth Experiments with AbMtlD Variants. For determining the growth defect caused by M1P accumulation, *A. baumannii* Δ*mtlD* strains complemented with the plasmid-borne AbMtlD variants (pBAVIK_*mtlD*_WT, pBAVIK_*mtlD*_D16A, pBAVIK_*mtlD*_D16A_D176A, and pBAVIK_*mtlD*_D16A_D176A_E175A) were streaked on agar plates containing minimal medium, 20 mM succinate as the sole carbon and energy source, 300 mM NaCl, and 50 μg/mL kanamycin as a selection marker. The plates were incubated overnight at 37 °C.

Quantification of M1P. Solutes were extracted as described before (17). The quantification of M1P was performed analogously to previous experiments with trehalose-6-phosphate (41). Mannitol concentrations were determined with the mannitol assay kit (K-MANOL, Megazyme).

SEC-MALS. SEC-MALS was performed at 4 °C using a TSK-GEL G3000SWXL column (15 mL; Tosoh Bioscience), a light-scattering detector (TREOS) and refractometer (Optilab rEX) from Wyatt Technology, and an ultraviolet detector, high-performance liquid chromatography pump, and degasser from Jasco. The system was equilibrated with three column volumes of buffer (buffer A: 20 mM HEPES pH 7.3, 300 mM NaCl, and 5 mM β-mercaptoethanol; buffer B: 20 mM Tris pH 7.3, 300 mM NaCl, and 5 mM β-mercaptoethanol; buffer C: 20 mM Tris pH 7.3, 600 mM NaCl, and 5 mM β-mercaptoethanol). All buffers were filtered through 0.1-μm pore–size Durapore polyvinylidene fluoride membrane filters (Merck) following recirculation through the system for 20 h at 0.5 mL/min to improve the baseline by removing air bubbles and particles by the degasser and preinjection filter (0.1 μm). Approximately 150 to 250 μg of protein in 100 μL of buffer was injected and analyzed at a flow rate of 0.5 mL/min. A light-scattering detector was calibrated by using monomeric bovine serum albumin (Merck). The obtained signals were processed with the ASTRA software package version 5.3.4.13 (Wyatt Technology). The concentration was determined by the refractometer using a refractive index increment (dn/dc) of 0.189 mL/g at 20.5 °C and 658 nm, as calculated by SEDFIT v16.1c (42).

Data Availability. The atomic coordinates and structure factors have been deposited in the Protein Data Bank (PDB) at http://www.pdb.org (PDB ID codes 7OCN, 7OCP, 7OCQ, 7OCR, 7OCS, 7OCT, and 7OCU). All other data are included in the manuscript and/or supporting information.

ACKNOWLEDGMENTS. This work was supported by a grant from the Deutsche Forschungsgemeinschaft through DFG Research Unit FOR 2251 "Adaptation and persistence of the emerging pathogen *Acinetobacter baumannii*." We acknowledge SOLEIL Synchrotron in Saint Aubin, France, for provision of the synchrotron radiation facilities. We would like to thank Dr. Leonard Chavas for assistance in using beamline PROXIMA 1 (proposal number 20181049) and Dr. Lidia Ciccone, Dr. William Shepard, and Dr. Martin Savko for assistance in using beamline PROXIMA 2A (proposal numbers 20170761, 20180035, and 20181049). The synchrotron trips to SOLEIL were partly supported by iNEXT, under PID 7108, funded by the Horizon 2020 programme of the European Union. We thank Ilona Rose for assistance in protein purification.

Author affiliations: [a]Institute of Biochemistry, Goethe University Frankfurt, Frankfurt am Main D-60438, Germany; [b]Department of Molecular Microbiology and Bioenergetics, Goethe University Frankfurt, Frankfurt am Main D-60438, Germany; and [c]Institute of Molecular Biosciences, Goethe University Frankfurt, Frankfurt am Main D-60438, Germany

Author contributions: H.-K.T. and S.H. designed research; H.-K.T., P.K., S.H., N.D.N., and R.A. performed research; H.-K.T. analyzed data; and H.-K.T., V.M., and K.M.P. wrote the paper.

1. L. Dijkshoorn, A. Nemec, H. Seifert, An increasing threat in hospitals: Multidrug-resistant *Acinetobacter baumannii*. *Nat. Rev. Microbiol.* **5**, 939–951 (2007).
2. A. Jawad, H. Seifert, A. M. Snelling, J. Heritage, P. M. Hawkey, Survival of *Acinetobacter baumannii* on dry surfaces: Comparison of outbreak and sporadic isolates. *J. Clin. Microbiol.* **36**, 1938–1941 (1998).
3. D. J. Morgan *et al.*, Frequent multidrug-resistant *Acinetobacter baumannii* contamination of gloves, gowns, and hands of healthcare workers. *Infect. Control Hosp. Epidemiol.* **31**, 716–721 (2010).
4. P.-E. Fournier *et al.*, Comparative genomics of multidrug resistance in *Acinetobacter baumannii*. *PLoS Genet.* **2**, e7 (2006).
5. P. Espinal, S. Martí, J. Vila, Effect of biofilm formation on the survival of *Acinetobacter baumannii* on dry surfaces. *J. Hosp. Infect.* **80**, 56–60 (2012).
6. A. Y. Peleg *et al.*, The success of *acinetobacter* species; genetic, metabolic and virulence attributes. *PLoS One* **7**, e46984 (2012).
7. I. Roca, P. Espinal, X. Vila-Farrés, J. Vila, The *Acinetobacter baumannii* oxymoron: Commensal hospital dweller turned pan-drug-resistant menace. *Front. Microbiol.* **3**, 148 (2012).
8. S. Zeidler, V. Müller, Coping with low water activities and osmotic stress in *Acinetobacter baumannii*: Significance, current status and perspectives. *Environ. Microbiol.* **21**, 2212–2230 (2019).
9. K. A. Tipton, C. Y. Chin, M. Farokhyfar, D. S. Weiss, P. N. Rather, Role of capsule in resistance to disinfectants, host antimicrobials, and desiccation in *Acinetobacter baumannii*. *Antimicrob. Agents Chemother.* **62**, e01188-18 (2018).
10. S. Zeidler, V. Müller, The role of compatible solutes in desiccation resistance of *Acinetobacter baumannii*. *MicrobiologyOpen* **8**, e00740 (2019).
11. J. M. H. Stoop, J. D. Williamson, D. M. Pharr, Mannitol metabolism in plants: A method for coping with stress. *Trends Plant Sci.* **1**, 139–144 (1996).
12. V. Chaturvedi, B. Wong, S. L. Newman, Oxidative killing of *Cryptococcus neoformans* by human neutrophils. Evidence that fungal mannitol protects by scavenging reactive oxygen intermediates. *J. Immunol.* **156**, 3836–3840 (1996).
13. M. Sand, A. I. Mingote, H. Santos, V. Müller, B. Averhoff, Mannitol, a compatible solute synthesized by *Acinetobacter baylyi* in a two-step pathway including a salt-induced and salt-dependent mannitol-1-phosphate dehydrogenase. *Environ. Microbiol.* **15**, 2187–2197 (2013).
14. T. Nguyen *et al.*, Targeting mannitol metabolism as an alternative antimicrobial strategy based on the structure-function study of mannitol-1-phosphate dehydrogenase in *Staphylococcus aureus*. *mBio* **10**, e02660-18 (2019).
15. B. Calmes *et al.*, Role of mannitol metabolism in the pathogenicity of the necrotrophic fungus *Alternaria brassicicola*. *Front. Plant Sci.* **4**, 131 (2013).
16. H. Zhao, Effect of ions and other compatible solutes on enzyme activity, and its implication for biocatalysis using ionic liquids. *J. Mol. Catal. B Enzym.* **37**, 16–25 (2005).
17. S. Zeidler *et al.*, Trehalose, a temperature- and salt-induced solute with implications in pathobiology of *Acinetobacter baumannii*. *Environ. Microbiol.* **19**, 5088–5099 (2017).
18. E. P. W. Kets, E. A. Galinski, M. de Wit, J. A. de Bont, H. J. Heipieper, Mannitol, a novel bacterial compatible solute in *Pseudomonas putida* S12. *J. Bacteriol.* **178**, 6665–6670 (1996).
19. M. Sand *et al.*, Mannitol-1-phosphate dehydrogenases/phosphatases: A family of novel bifunctional enzymes for bacterial adaptation to osmotic stress. *Environ. Microbiol.* **17**, 711–719 (2015).
20. S. Zeidler *et al.*, Salt induction and activation of MtlD, the key enzyme in the synthesis of the compatible solute mannitol in *Acinetobacter baumannii*. *MicrobiologyOpen* **7**, e00614 (2018).
21. J. D. Selengut, MDP-1 is a new and distinct member of the haloacid dehalogenase family of aspartate-dependent phosphohydrolases. *Biochemistry* **40**, 12704–12711 (2001).
22. J.-F. Collet, V. Stroobant, M. Pirard, G. Delpierre, E. Van Schaftingen, A new class of phosphotransferases phosphorylated on an aspartate residue in an amino-terminal DXDX(T/V) motif. *J. Biol. Chem.* **273**, 14107–14112 (1998).
23. H. W. Wisselink *et al.*, Mannitol production by lactic acid bacteria: A review. *Int. Dairy J.* **12**, 151–161 (2002).
24. S. D. Lahiri, G. Zhang, J. Dai, D. Dunaway-Mariano, K. N. Allen, Analysis of the substrate specificity loop of the HAD superfamily cap domain. *Biochemistry* **43**, 2812–2820 (2004).
25. M. Klimacek, K. L. Kavanagh, D. K. Wilson, B. Nidetzky, *Pseudomonas fluorescens* mannitol 2-dehydrogenase and the family of polyol-specific long-chain dehydrogenases/reductases: Sequence-based classification and analysis of structure-function relationships. *Chem. Biol. Interact.* **143-144**, 559–582 (2003).
26. M. Klimacek, B. Nidetzky, A catalytic consensus motif for D-mannitol 2-dehydrogenase, a member of a polyol-specific long-chain dehydrogenase family, revealed by kinetic characterization of site-directed mutants of the enzyme from *Pseudomonas fluorescens*. *Biochem. J.* **367**, 13–18 (2002).
27. K. L. Kavanagh, M. Klimacek, B. Nidetzky, D. K. Wilson, Crystal structure of *Pseudomonas fluorescens* mannitol 2-dehydrogenase binary and ternary complexes. Specificity and catalytic mechanism. *J. Biol. Chem.* **277**, 43433–43442 (2002).
28. S. Krahulec, G. C. Armao, M. Klimacek, B. Nidetzky, Enzymes of mannitol metabolism in the human pathogenic fungus *Aspergillus fumigatus*–Kinetic properties of mannitol-1-phosphate 5-dehydrogenase and mannitol 2-dehydrogenase, and their physiological implications. *FEBS J.* **278**, 1264–1276 (2011).
29. D. Berkowitz, D-Mannitol utilization in *Salmonella typhimurium*. *J. Bacteriol.* **105**, 232–240 (1971).
30. E. Solomon, E. C. C. Lin, Mutations affecting the dissimilation of mannitol by *Escherichia coli* K-12. *J. Bacteriol.* **111**, 566–574 (1972).
31. D. Szatmári *et al.*, Intracellular ion concentrations and cation-dependent remodelling of bacterial MreB assemblies. *Sci. Rep.* **10**, 12002 (2020).
32. L. Shabala *et al.*, Ion transport and osmotic adjustment in *Escherichia coli* in response to ionic and non-ionic osmotica. *Environ. Microbiol.* **11**, 137–148 (2009).

33. A. M. Whatmore, J. A. Chudek, R. H. Reed, The effects of osmotic upshock on the intracellular solute pools of *Bacillus subtilis*. *J. Gen. Microbiol.* **136**, 2527–2535 (1990).
34. G. D. Van Duyne, R. F. Standaert, P. A. Karplus, S. L. Schreiber, J. Clardy, Atomic structures of the human immunophilin FKBP-12 complexes with FK506 and rapamycin. *J. Mol. Biol.* **229**, 105–124 (1993).
35. W. Kabsch, XDS. *Acta Crystallogr. D Biol. Crystallogr.* **66**, 125–132 (2010).
36. P. Skubák, N. S. Pannu, Automatic protein structure solution from weak X-ray data. *Nat. Commun.* **4**, 2777 (2013).
37. P. Emsley, B. Lohkamp, W. G. Scott, K. Cowtan, Features and development of *Coot*. *Acta Crystallogr. D Biol. Crystallogr.* **66**, 486–501 (2010).
38. G. N. Murshudov *et al.*, *REFMAC*5 for the refinement of macromolecular crystal structures. *Acta Crystallogr. D Biol. Crystallogr.* **67**, 355–367 (2011).
39. V. B. Chen *et al.*, MolProbity: All-atom structure validation for macromolecular crystallography. *Acta Crystallogr. D Biol. Crystallogr.* **66**, 12–21 (2010).
40. D. Liebschner *et al.*, Polder maps: Improving OMIT maps by excluding bulk solvent. *Acta Crystallogr. D Struct. Biol.* **73**, 148–157 (2017).
41. J. J. Hubloher *et al.*, Trehalose-6-phosphate-mediated phenotypic change in *Acinetobacter baumannii*. *Environ. Microbiol.* **22**, 5156–5166 (2020).
42. H. Zhao, E. Casillas Jr., H. Shroff, G. H. Patterson, P. Schuck, Tools for the quantitative analysis of sedimentation boundaries detected by fluorescence optical analytical ultracentrifugation. *PLoS One* **8**, e77245 (2013).
43. E. Chovancova *et al.*, CAVER 3.0: A tool for the analysis of transport pathways in dynamic protein structures. *PLOS Comput. Biol.* **8**, e1002708 (2012).